JOURNAL OF CHEMICAL PHYSICS VOLUME 121, NUMBER 10 8 SEPTEMBER 2004

Theoretical study of excitations in furan: Spectra and molecular dynamics

E. V. Gromov, A. B. Trofimov, and N. M. Vitkovskaya
Laboratory of Quantum Chemistry, Computer Center, Irkutsk State University, 664003 Irkutsk, Russian Federation

H. Köppel, J. Schirmer, H.-D. Meyer, and L. S. Cederbaum
Theoretische Chemie, Physikalisch-Chemisches Institut, Universität Heidelberg, Im Neuenheimer Feld 229, D-69120 Heidelberg, Germany

(Received 19 February 2004; accepted 16 June 2004)

The excitation spectra and molecular dynamics of furan associated with its low-lying excited singlet states $^1A_2(3s)$, $^1B_2(V)$, $^1A_1(V')$, and $^1B_1(3p)$ are investigated using an *ab initio* quantum-dynamical approach. The *ab initio* results of our previous work [J. Chem. Phys. **119**, 737 (2003)] on the potential energy surfaces (PES) of these states indicate that they are vibronically coupled with each other and subject to conical intersections. This should give rise to complex nonadiabatic nuclear dynamics. In the present work the dynamical problem is treated using adequate vibronic coupling models accounting for up to four coupled PES and thirteen vibrational degrees of freedom. The calculations were performed using the multiconfiguration time-dependent Hartree method for wave-packet propagation. It is found that in the low-energy region the nuclear dynamics of furan is governed mainly by vibronic coupling of the $^1A_2(3s)$ and $^1B_2(V)$ states, involving also the $^1A_1(V')$ state. These interactions are responsible for the ultrafast internal conversion from the $^1B_2(V)$ state, characterized by a transfer of the electronic population to the $^1A_2(3s)$ state on a time scale of ~25 fs. The calculated photoabsorption spectrum of furan is in good qualitative agreement with experimental data. Some assignments of the measured spectrum are proposed. © *2004 American Institute of Physics.* [DOI: 10.1063/1.1780160]

I. INTRODUCTION

The rapid progress in the excited-state molecular studies, stimulated in recent years by the remarkable advances in the experimental techniques,[1] revealed the paramount importance of nonadiabatic effects for a variety of excited-state dynamical processes.[2–7] The ultrafast internal conversion, radiationless decay, and complex (vibronic) structure of absorption spectra are common examples of such effects in the excited molecules.[2–4] As is now generally recognized, conical intersections of the electronic potential energy surfaces (PES) play central role in these phenomena, which are the points in the nuclear coordinate space where the adiabatic PES become degenerate.[3,6,7] The information about conical intersections gained from examination of the excited-state PES helps to formulate sensible models that can be further used for the investigation of the excited-state dynamics.

Recently, we have performed a detailed theoretical study of the low-lying excited singlet states of furan (C_4H_4O) (Ref. 8) (Paper I). The PES of the lowest two Rydberg [$^1A_2(3s)$,$^1B_1(3p)$], and two π-π^* valence [$^1B_2(V)$,$^1A_1(V')$] states were examined in the vicinity of the equilibrium ground-state molecular configuration using the equation-of-motion coupled-cluster singles and doubles (EOM-CCSD) method. According to our results, the PES of these states form multiple conical intersections with each other, so that extensive nonadiabatic effects can be expected in the low-energy photophysics and photochemistry of furan. Indeed, the lowest absorption band in the vacuum ultraviolet (VUV) spectrum of furan (located in the 5.7–6.5 eV region) has an appearance typical for the situation, where nonadiabatic effects are important: the spectrum is diffuse and shows scarce and irregular vibronic structure. It is therefore not surprising that, despite many experimental[9–24] and theoretical[25–34] studies, this part of the excitation spectrum is still rather poorly understood. Our results (Paper I) predict that within the considered energy range the most important coupling schemes are $^1A_2 \times b_1 \times {}^1B_2$ and $^1B_2 \times b_2 \times {}^1A_1$. These interactions are the key to understanding the low-energy singlet excited-state nuclear dynamics of furan.

In the present work we study the spectroscopy and molecular dynamics of furan related to the $^1A_2(3s)$, $^1B_2(V)$, $^1A_1(V')$, and $^1B_1(3p)$ excited states. This study is based on our earlier paper, Paper I, which provided the potential energy surfaces and electronic structural data relevant to the present work. However, neither spectroscopic nor time-dependent dynamical calculations were performed in Paper I. In the first place we compute and compare with experiment the relevant part of the excitation spectrum. This allows us to assess the quality of our model and to clarify some of the spectroscopic issues. Starting with the most important vibronic interactions established in Paper I, we investigate the role of the other vibronic coupling schemes for the spectrum. We study also the relaxation processes taking place after photoexcitation to the $^1B_2(V)$ state.

We make use of the vibronic coupling formalism based on the concept of vibronic model Hamiltonians for diabatic electronic states.[3] This approach proved to be very useful in many earlier and recent dynamical studies.[2,3,35–39] We use the linear vibronic coupling (LVC) approximation, in which only coupling terms linear in nuclear coordinates are retained in the Hamiltonian. The approach allows to treat simultaneously several electronic states and many vibrational degrees of freedom—our model Hamiltonian accounts for 4 states and 13 vibrational modes. The model is parametrized using the results of *ab initio* calculations, reported in Paper I. The Heidelberg multiconfiguration time-dependent Hartree (MCTDH) package for wave-packet propagation[40] is employed to solve the dynamical problems. The MCTDH method[41,42] suits very well for the treatment of large vibronic coupling problems and was successfully used in similar studies.[36–39] One of the advantages of the MCTDH method is its high efficiency with respect to the number of nuclear degrees of freedom that can be treated in the calculations. Examples of the remarkable performance of the MCTDH method are the dynamical study of pyrazine[36] (24 nuclear degrees of freedom), investigation on a system bath model[43] (up to 61 degrees of freedom), and studies on the spin-boson model[44–46] (up to 1000 degrees of freedom). Returning to the furan problem we note that for the reduced models we also use a conventional time-independent approach consisting in Lanczos diagonalization of the Hamiltonian expressed in a ground-state harmonic oscillator basis.[3]

II. THEORETICAL FRAMEWORK

A. Model Hamiltonian

To tackle the nonadiabatic nuclear dynamics of furan on the manifold of its low-lying excited states $^1A_2(3s)$, $^1B_2(V)$, $^1B_1(3p)$, and $^1A_1(V')$, we use the approach in which the vibronic Hamiltonian is formulated in the basis of *diabatic* electronic states.[47] This considerably simplifies the formulation and treatment of the vibronic coupling problem at all stages.[3,4] The simplifications in the diabatic basis arise due to the fact that the nonadiabatic coupling of the electronic states is introduced here via the potential energy rather than via the kinetic energy of the nuclei. A Taylor expansion of the potential energy through linear terms in nuclear coordinates yields the so-called LVC Hamiltonian.[3,4] For our four-state problem the LVC Hamiltonian reads

$$\mathbf{H}=H_0\mathbf{1}+\begin{pmatrix} E(A_2)+\sum_{s\in a_1} k_s^1 Q_s & \sum_{s\in b_1}\lambda_s^{12}Q_s & \sum_{s\in a_2}\lambda_s^{13}Q_s & \sum_{s\in b_2}\lambda_s^{14}Q_s \\ \sum_{s\in b_1}\lambda_s^{12}Q_s & E(B_2)+\sum_{s\in a_1} k_s^2 Q_s & \sum_{s\in b_2}\lambda_s^{23}Q_s & \sum_{s\in a_2}\lambda_s^{24}Q_s \\ \sum_{s\in a_2}\lambda_s^{13}Q_s & \sum_{s\in b_2}\lambda_s^{23}Q_s & E(A_1)+\sum_{s\in a_1} k_s^3 Q_s & \sum_{s\in b_1}\lambda_s^{34}Q_s \\ \sum_{s\in b_2}\lambda_s^{14}Q_s & \sum_{s\in a_2}\lambda_s^{24}Q_s & \sum_{s\in b_1}\lambda_s^{34}Q_s & E(B_1)+\sum_{s\in a_1} k_s^4 Q_s \end{pmatrix}. \tag{1}$$

In this expression $\mathbf{1}$ is the 4×4 unit matrix; $E(A_2)$, $E(B_2)$, $E(A_1)$, and $E(B_1)$ are the vertical energies of the respective singlet excited states; k_s^i and λ_s^{ij} denote parameters of the LVC Hamiltonian referred to as the *intrastate* and *interstate* coupling constants, respectively. The summations run over the vibrational normal modes of the specified symmetry. Q_s denote the dimensionless normal coordinates in the electronic ground state.[48–50] H_0 is the vibrational Hamiltonian of the electronic ground state,

$$H_0=\frac{1}{2}\sum_s \omega_s\left(\frac{\partial^2}{\partial Q_s^2}+Q_s^2-1\right), \tag{2}$$

describing noninteracting harmonic oscillators with frequencies ω_s. In the Hamiltonian H_0 the vibrational ground-state energy is taken as the origin of the energy scale. The coupling constants k_s^i and λ_s^{ij}, as well as the excitation energies $E(i)$ and frequencies ω_s, represent parameters of the model and have to be determined in a suitable way.

B. Parameters of the model

In Tables I and II we list the full set of parameters entering the LVC Hamiltonian of Eq. (1). All parameters were determined from the results of our *ab initio* calculations.[8] We recall that in these calculations the EOM-CCSD method[51] and Dunning's cc-pVDZ basis[52] augmented by diffuse functions were employed. The ground-state vibrational frequencies and the corresponding normal vibrational modes were computed at the level of the second-order Møller-Plesset perturbation theory (MP2). The normal modes are labeled according to Mellouki *et al.*[53]

The vertical ordering of the states at the ground-state equilibrium geometry can be seen from Table I. The $^1A_1(V')$ state vertically appears to be the fifth lowest excited state. However, as found in Paper I, its energy depends strongly on the nuclear coordinates and for distorted geometries it is often found below the $^1A_2(3p)$ state. By contrast, the excitation energy of the latter state does not change much with the

TABLE I. EOM-CCSD energies E (eV) and oscillator strengths f of the vertical transitions to the five lowest singlet excited states of furan.

	$^1A_2(3s)$	$^1B_2(V)$	$^1B_1(3p)$	$^1A_2(3p)$	$^1A_1(V')$
E	6.01	6.44	6.53	6.69	6.72
f		0.166	0.036		<0.001

TABLE II. EOM-CCSD vibronic coupling constants k and λ (eV), MP2 ground-state vibrational frequencies ω (eV), and Poisson excitation parameters a for vibrational normal modes in the lowest excited states of furan. In parentheses are shown results of the ADC(2) calculations.[a]

Mode a_1	ω	a	$^1A_2(3s)$ k_s^1	$^1B_2(V)$ k_s^2	$^1A_1(V')$ k_s^3	$^1B_1(3p)$ k_s^4
ν_1	0.4132	0.014	−0.017(−0.024)	0.018(0.007)	0.070(0.068)	−0.010(−0.018)
ν_2	0.4099	0.000	−0.008(−0.010)	0.004(0.003)	0.009(0.008)	0.002(−0.001)
ν_3	0.1885	0.894	−0.155(−0.146)	−0.192(−0.185)	−0.252(−0.219)	−0.169(−0.157)
ν_4	0.1773	0.722	0.130(0.112)	0.213(0.177)	0.107(0.095)	0.129(0.109)
ν_5	0.1443	0.951	−0.002(−0.001)	−0.063(−0.045)	−0.199(−0.201)	−0.006(−0.003)
ν_6	0.1384	0.299	0.107(0.107)	0.067(0.079)	−0.017(−0.066)	0.075(0.076)
ν_7	0.1265	0.344	0.044(0.038)	0.105(0.082)	0.032(0.054)	0.027(0.023)
ν_8	0.1085	0.214	−0.056(−0.057)	−0.071(−0.062)	0.016(0.025)	−0.048(−0.047)
a_2			$\lambda_s^{13}(^1A_2\text{-}^1A_1)$		$\lambda_s^{24}(^1B_2\text{-}^1B_1)$	
ν_9	0.1045	0.033	0.0		0.027	
ν_{10}	0.0892	0.139	0.0		0.047	
ν_{11}	0.0743	1.219	0.116(0.100)		0.061	
b_1			$\lambda_s^{12}(^1A_2\text{-}^1B_2)$		$\lambda_s^{34}(^1A_1\text{-}^1B_1)$	
ν_{12}	0.1022	0.0	0.0		0.0	
ν_{13}	0.0937	0.115	0.045(0.038)		0.0	
ν_{14}	0.0779	0.808	0.099(0.088)		0.058	
b_2			$\lambda_s^{14}(^1A_2\text{-}^1B_1)$		$\lambda_s^{23}(^1B_2\text{-}^1A_1)$	
ν_{15}	0.4123	0.0	0.0		0.0	
ν_{16}	0.4085	0.0	0.0		0.0	
ν_{17}	0.1966	0.162	0.112(0.113)		0.106	
ν_{18}	0.1589	0.081	0.044		0.064	
ν_{19}	0.1549	0.653	0.122(0.140)		0.177	
ν_{20}	0.1314	0.181	0.028		0.079	
ν_{21}	0.1089	0.213	0.052(0.069)		0.071	

[a] In case of k_s^1-k_s^4, taken from Ref. 29.

geometry, so that it is not expected to seriously influence the lowest part of the excitation spectrum. The $^1A_2(3p)$ state was therefore neglected in the present study.

The vibronic coupling constants k_s^i and λ_s^{ij} were determined according to the expressions presented in our earlier work,[35,54] which were obtained using relations described in Ref. 3. The results are shown in Table II. Where possible, we show for comparison also the results of our previous polarization propagator calculations[29] (the constants λ_s^{ij} were not published in Ref. 29). As can be seen, the two sets of constants are in good agreement with each other. Somewhat larger discrepancies are found for k_s^i of the $^1B_2(V)$ and $^1A_1(V')$ states, which is not unexpected, in view of the more complex valence nature of these states. Another observation is that the coupling constants for the models ν_1, ν_2, ν_9, ν_{10}, ν_{12}, ν_{13}, ν_{15}, and ν_{16} describing essentially motion of hydrogen atoms are relatively small. These modes were neglected in all our dynamical calculations reported below.

C. Calculation of the spectra

1. Time-independent approach

Within the present time-independent treatment of the vibronic problem the final state $|\Psi_m\rangle$ is expanded in terms of the diabatic electronic states $|\Phi_i\rangle$ (Ref. 3):

$$|\Psi_m(\mathbf{r},\mathbf{Q})\rangle=\sum_i |\chi_{im}(\mathbf{Q})\rangle|\Phi_i(\mathbf{r},\mathbf{Q})\rangle, \tag{3}$$

where the summation runs over all vibronically coupled electronic states, and $\mathbf{r}$ and $\mathbf{Q}$ denote the electronic and nuclear coordinates, respectively. The expansion coefficients $|\chi_{im}\rangle$ (vibrational wavefunctions) are determined from the eigenvalue problem for the matrix LVC Hamiltonian $\mathbf{H}$,

$$\mathbf{H}\boldsymbol{\chi}_m=E_m\boldsymbol{\chi}_m, \tag{4}$$

where E_m are the excitation energies for the final vibronic states $|\Psi_m\rangle$.

Equation (4) can be solved using a variational ansatz in which the vibrational wave functions $|\chi_{im}\rangle$ are expanded in a direct-product basis $|n_1,\dots,n_M\rangle$ of harmonic oscillator eigenstates of H_0,

$$|\chi_{im}\rangle=\sum_{n_1,\dots,n_M} C_{im}^{n_1,\dots,n_M}|n_1,\dots,n_M\rangle. \tag{5}$$

Here the summation comprises all possible combinations of quantum numbers for the individual modes (M is the total number of modes). In practice, of course, one has to restrict the expansion [Eq. (5)] by specifying maximal excitation levels for the normal modes ν_s.

Once the vibrational wave functions $|\chi_{im}\rangle$ and excitation energies E_m are known, the spectral function describing the excitation from the zero vibrational level $|\chi_{00}\rangle$ of the electronic ground state $|\Phi_0\rangle$ into the manifold of vibronically interacting states $|\Phi_i\rangle$ can be evaluated according to Fermi's golden rule

$$P(E)=\sum_i \sum_m f_{0i}|\langle \chi_{00}|\chi_{im}\rangle|^2 \delta(E-E_m), \tag{6}$$

where f_{0i} is the oscillator strength for the electronic state $|\Phi_i\rangle$. The particularly simple appearance of Eq. (6) is due to the Franck-Condon approximation which is roughly valid for the diabatic electronic states employed here.

In the limit of noninteracting states [that is, when all λ^s_{ij} in Eq. (1) vanish] Eq. (6) reduces to a superposition of vibrational progressions,[3,50]

$$P(E)=\sum_i f_{0i} \sum_{n_1,\ldots,n_g} |\langle 0,...,0|n_1,\ldots,n_g\rangle|^2 \times \delta\left(E-E_i+\sum_s \omega_s(a_{is}-n_s)\right), \tag{7}$$

where only totally symmetric normal modes ($s=1,2,...,g$) are accounted for. Here each progression represents the spectrum of a shifted harmonic oscillator (described by a Poisson intensity distribution). The Franck-Condon factors in Eq. (7) read

$$|\langle 0,...,0|n_1,\ldots,n_g\rangle|^2=\prod_{s\in g} \frac{(a_{is})^{n_s}}{n_s!} e^{-a_{is}}, \tag{8}$$

where $a_{is}=\frac{1}{2}(\kappa^s_i/\omega_s)^2$ is the so-called Poisson (or vibrational strength) parameter.

For the evaluation of the spectrum according to Eq. (6) it is decisive that the overlaps $\langle \chi_{00}|\chi_{im}\rangle$, determining the intensity of the vibronic lines, can be calculated without fully solving the eigenvalue problem of Eq. (4). To this end, a specific variant of the Lanczos algorithm is employed.[3]

2. Wave-packet dynamics using the MCTDH method

The MCTDH method represents an efficient approach for the solution of the time-dependent Schrödinger equation.[41,42] In the MCTDH scheme the time-dependent wave function can be written as follows:

$$|\Psi(\mathbf{r},\mathbf{Q},t)\rangle=\sum_i |\chi_i^{\mathrm{MCTDH}}(\mathbf{Q},t)\rangle|\Phi_i(\mathbf{r},\mathbf{Q})\rangle, \tag{9}$$

where, as in Eq. (3), the summation is performed over the set of interacting electronic states $|\Phi_i\rangle$ and the expansion coefficients $|\chi_i^{\mathrm{MCTDH}}\rangle$ are vibrational wave functions. The latter quantities are, however, now time dependent and subject to further expansion in terms of the time-dependent basis functions and coefficients,

$$|\chi_i^{\mathrm{MCTDH}}(\mathbf{Q},t)\rangle=\sum_{n_1,\ldots,n_P} A^{(i)}_{n_1,\ldots,n_p}(t)\prod_{j=1}^{P} |\varphi^{(i,j)}_{n_j}(\mathbf{q}_j,t)\rangle. \tag{10}$$

The MCTDH wave function is thus a time-dependent superposition of time-dependent configurations which are (Hartree-) products of single-particle functions $|\varphi^{(i,j)}_{n_j}\rangle$. These single-particle functions may be one-dimensional or multidimensional and their arguments q_j denote one or a collection of several modes of the original coordinates, i.e.

$$Q=(Q_1,\ldots,Q_N)=(q_j,\ldots,q_p). \tag{11}$$

This mode combination technique is important to further reduce the size of the problem. The optimal number of MCTDH particles or combined modes lies, in general, between $P=3$ and $P=6$.

The MCTDH EOM follow from applying a variational principle to Eq. (10). These EOM form a set of coupled nonlinear, first-order differential equations.[41,42] Although these EOM are complicated, their use is of advantage because there are much fewer equations to be solved as in competing methods. This follows from the fact that the basis of single-particle functions moves—variationally optimized—with the wave packet, which leads to a rather fast convergence in this basis.

The technical solution of the EOM for the single-particle functions requires that they are represented by a time-independent primitive basis. For this we choose a discrete variable representation (DVR) (Ref. 55) and use product grids for combined modes.

Within the time-dependent formalism the spectral envelope is evaluated according to

$$P(E)=\sum_i f_{0i}P_i(E),$$
$$P_i(E)\propto E\,\mathrm{Re}\int_0^\infty e^{iEt}C_i(t)dt, \quad C_i(t)=\langle \Psi_i(0)|\Psi_i(t)\rangle, \tag{12}$$

where $C(t)$ denotes the autocorrelation function. The initial state $\Psi_i(0)$ is the ground-state vibrational wave function placed on the *i*th diabatic electronic state. The autocorrelation function is evaluated as

$$C_i(t)=\langle \Psi_i^*(t/2)|\Psi_i(t/2)\rangle, \tag{13}$$

which is valid for a real initial state and symmetric Hamiltonian. This and other technical details are discussed in Ref. 42.

3. Technical details

In Table III we summarize the details of the present MCTDH calculations. The single-particle function (SPF) basis, depending on the final vibronic symmetry, comprises from 10 to 18 SPFs for each electronic state. The 13 active vibrational modes were combined into 5 particles, as shown in the first column. The SPFs were represented in terms of harmonic oscillator DVR.[55] The number of grid points taken for each normal mode is shown in the second column of Table III. The initial wave function was taken as the ground state vibrational wave function. The size of the primitive and single-particle basis sets was selected so that the resulting spectrum is converged with respect to the number of terms in the expansion, i.e., the spectral envelope does not change within plotting accuracy on adding functions. The effect of the experimental resolution was added to the calculated spectra by damping the autocorrelation function by a suitable time-dependent function.[42] In the present work we choose an exponential damping with a characteristic time of 33 fs, which yields a Lorentzian broadening of the spectra with a full width at half maximum (FWHM) of ~0.04 eV. The same FWHM was used for plotting the spectra computed within the time-independent approach.

TABLE III. Details of the MCTDH calculations. The first column displays vibrational modes combined together which were treated as a single particle. The second column displays the numbers of DVR grid points for the individual degrees of freedom. The single-particle functions are propagated on the corresponding product grid. The last four columns display the number of single-particle functions employed for each electronic state.

Combination scheme for SPF	Number of primitive grid points	Number of SPF[a]			
		$^1A_2(3s)$	$^1B_2(V)$	$^1A_1(V')$	$^1B_1(3p)$
(ν_8,ν_7,ν_6)	(7,7,8)	12	12	10	10
(ν_5,ν_4,ν_3)	(8,10,10)	14	14	12	12
$(\nu_{21},\nu_{20},\nu_{18})$	(9,8,6)	12 [14]	12	10	10
(ν_{19},ν_{17})	(12,7)	14 [13]	14 [13]	12 [11]	12 [11]
(ν_{11},ν_{14})	(14,12)	14 [18]	14	12	12

[a] In brackets are given the numbers of SPFs for the case of B_1 vibronic symmetry if different from those for the case of B_2 vibronic symmetry.

The time-independent Lanczos calculations were carried out to obtain energies and intensities of the individual vibronic transitions (i.e., so-called ‘‘bar’’ spectra) in cases where such information represented interest for the analysis. In these calculations the number of harmonic oscillator basis states was also carefully chosen, to ensure convergence of the spectra, while keeping the overall size of the basis possibly small. The dimension of the largest Hamiltonian matrix was about 5×10^7. The spectra were computed using 5000 Lanczos iteration steps. The converged spectra were checked against the results of the MCTDH method.

III. RESULTS AND DISCUSSION

A. The adiabatic potential energy surfaces

The adiabatic PES are obtained as eigenvalues of the potential energy part of the vibronic Hamiltonian [Eq. (1)]. Since the present work deals with the excited-state molecular dynamics, it is useful to take a closer look at the relevant PES. First we discuss on the geometrical parameters and excitation energies of furan predicted by the present model for several excited-state stationary points [useful formulas for extracting such information from LVC model can be found in Refs. 3 and 37(a)]. The results are shown in Tables IV and V in comparison with the full geometry optimization calculations (Paper I). As can be seen, nearly all present geometrical characteristics (Table IV) agree very well with those of the optimized structures. For the $^1A'(V)$ stationary point the maximum deviations for bond lengths and valence angles are 0.06 Å and 2°, respectively. For all other structures they are less than 0.01 Å and 1°. Regarding excitation energies (Table V) the agreement between the model results and *ab initio* calculations is also very good. For most excitation energies the discrepancy is less than 0.03 eV, with few exceptions in the case of the $^1A'(V)$ structure. The above emphasizes the reliability of our LVC model.

TABLE IV. Comparison of the present LVC model and fully optimized[a] (Opt.) geometrical parameters of furan (bond length in Å and angles in deg) at various excited-state stationary points.[b]

	$^1A_2(3s)$		$^1B_2(V)$		$^1A'(V)$[c]		$^1B_1(3p)$		$^1A_1(V')$	
Parameter	Model	Opt.	Model	Opt.	Model	Opt.	Model	Opt.	Model	Opt.
Bond lengths										
O-C$_2$	1.353	1.352	1.378	1.387	1.316	1.320	1.355	1.354	1.380	1.378
					(1.442)	(1.500)				
C$_2$-C$_3$	1.417	1.417	1.440	1.443	1.457	1.455	1.418	1.419	1.452	1.460
					(1.430)	(1.427)				
C$_3$-C$_{3'}$	1.389	1.393	1.373	1.383	1.396	1.404	1.398	1.398	1.457	1.464
C$_2$-H$_2$	1.089	1.091	1.089	1.089	1.090	1.091	1.091	1.091	1.084	1.085
					(1.087)	(1.087)				
C$_3$-H$_3$	1.089	1.092	1.088	1.089	1.090	1.089	1.091	1.091	1.088	1.088
					(1.089)	(1.087)				
Angles										
C$_{2'}$-O-C$_2$	106.2	106.2	105.8	104.7	106.9	104.8	106.8	106.7	109.8	109.6
O-C$_2$-C$_3$	111.0	111.2	110.4	111.3	111.1	112.8	110.7	110.8	109.1	109.6
					(109.0)	(108.8)				
C$_2$-C$_3$-C$_{3'}$	105.9	105.7	105.8	106.4	106.8	107.1	105.9	105.8	106.0	105.8
					(106.1)	(106.5)				
O-C$_2$-H$_2$	116.6	116.4	116.4	116.0	117.7	117.3	117.3	117.1	116.5	116.6
					(115.1)	(113.9)				
C$_2$-C$_3$-H$_3$	125.3	125.5	124.7	124.8	123.8	124.1	124.4	124.6	126.4	124.6
					(126.6)	(125.8)				

[a] EOM-CCSD calculations from Ref. 8.

[b] Nomenclature of stationary points and geometrical parameters from Ref. 8.

[c] There are two sets of O-C$_2$, etc., structural parameters in the case of $^1A'(V)$ stationary point because of its lower (C_s) symmetry (see Ref. 8 for more details).

TABLE V. Comparison of the present LVC model and fully optimized[a] (Opt.) excitation energies (eV) of furan at geometries of various excited-state stationary points of Table IV.

Stationary point		$^1A_2(3s)$		$^1B_2(V)$		$^1B_1(3p)$		$^1A_1(V')$	
		Model	Opt.	Model	Opt.	Model	Opt.	Model	Opt.
$^1A_2(3s)$	C_{2v} min	5.84	5.84	6.17	6.18	6.38	6.38	6.62	6.62
$^1B_2(V)$	C_{2v} saddle	5.90	5.93	6.12	6.11	6.43	6.46	6.56	6.56
$^1A'(V)$	C_s saddle	5.97	6.09	6.07	6.07	6.68	6.61	6.83	6.82
$^1B_1(3p)$	C_{2v} min	5.85	5.85	6.18	6.18	6.37	6.37	6.58	6.58
$^1A_1(V')$	C_{2v} saddle	6.08	6.11	6.30	6.31	6.57	6.59	6.38	6.36

[a] EOM-CCSD calculations from Ref. 8.

The present four-state model reproduces all features of the PES described in Paper I. The most important of them for the present work are conical intersections of PES. In Fig. 1 one can see several of such intersections as curve crossings of the $^1A_2(3s)$, $^1B_2(V)$, $^1A_1(V')$, and $^1B_1(3p)$ PES along the normal coordinate of the totally symmetric ν_5 mode. Similar cuts can be made for the a_1 modes ν_3, ν_4, and $\nu_6-\nu_8$. Taking all a_1 modes into account, one can estimate the minimum energy of each conical intersection (Table VI).[3] The lowest of these energies [intersection of the $^1A_2(3s)$ and $^1B_2(V)$ PES] is 6.32 eV.

Let us now consider the effect of the nontotally symmetric modes. There is strong vibronic coupling via the b_2 modes between the $^1B_2(V)$ and $^1A_1(V')$ states (coupling scheme $^1B_2 \times b_2 \times {}^1A_1$) and more moderate one between $^1A_2(3s)$ and $^1B_1(3p)$ states ($^1A_2 \times b_2 \times {}^1B_1$). Effect of these couplings is demonstrated in Fig. 2. In the plot one sees that whereas the PES of $^1A_2(3s)$ state only flattens due to the interaction with the $^1B_1(3p)$ state, the $^1B_2(V)$ potential develops a global double-well shape, resulting from the repulsion of $^1B_2(V)$ and $^1A_1(V')$ PES. Interestingly, such behavior of the $^1B_2(V)$ potential leads to its intersection with the $^1A_2(3s)$ one. The intersection is, however, unusual, since it involves b_2 modes, which act as additional "tuning" modes. As a result of such tuning the $^1B_2$-$^1A_2$ intersection occurs at much lower energy (~6.18 eV) than if accounting for only totally symmetric modes (6.32 eV). Here we note that dropping the $^1A_2(3s)$-$^1B_1(3p)$ coupling leads to a small shift of the $^1B_2$-$^1A_2$ crossing energy, namely, the energy is about 6.08 eV as predicted in Paper I.

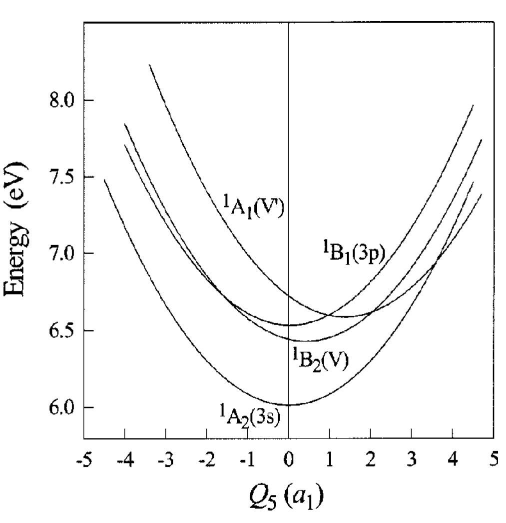

FIG. 1. LVC model potential energy curves for totally symmetric normal coordinate Q_5. The other normal coordinates are set to zero.

The coupling between the $^1B_2(V)$ and $^1A_2(3s)$, and the $^1A_1(V')$ and $^1B_1(3p)$, states along the b_1 (ν_{14}) mode has moderate strength. At the minimum of the $^1A_2(3s)$ state the lowest PES is flattened by the interaction, but retains a single-well shape (Paper I). The situation is, however, different in the vicinity of the conical intersection of the $S_1(^1A_2)$ and $S_2(^1B_2)$ PES involving b_2 modes. Here, the lower potential develops a local double-well character along the b_1 (ν_{14}) mode. This situation is very well seen in the three-dimensional view of the S_1 and S_2 PES in Fig. 3.

The present model goes beyond the prototype model used in Paper I as it includes the a_2 mode (ν_{11}), which couples the $^1A_2(3s)$ and $^1A_1(V')$, and the $^1B_2(V)$ and $^1B_1(3p)$ states. The $^1A_2 \times a_2 \times {}^1A_1$ interaction causes only certain flattening of the $^1A_2(3s)$ PES near its minimum. What, however, is more interesting, is that the a_2 mode in combination with the b_2 modes enables an *indirect* coupling of the $^1A_2(3s)$ and $^1B_2(V)$ states: $^1A_2 \times [a_2 \times b_2] \times {}^1B_2$ (an analysis of this coupling scheme is given in the Appendix). The *indirect* coupling of the $^1A_2(3s)$ and $^1B_2(V)$ states leads to a conical intersection of the corresponding PES in the space of the a_1, b_2, and a_2 modes,[56] accompanied by the development of a local double-well lower surface near the intersection point. The situation formally resembles the conical intersection of the $^1A_2(3s)$ and $^1B_2(V)$ PES in the space of the a_1, b_2, and b_1 modes (see Fig. 3 substituting b_1 by a_2) resulting from the *direct* interaction of these states.

Concluding this section we note that the present four-state model is more realistic and complete than the prototype model of Paper I. Being consistent with the latter it also covers the *indirect* coupling and accounts for the interactions with the $^1B_1(3p)$ excited state. This results in a better description of the PES in the vicinity of the Franck-Condon zone which is known to be very important for reproducing the experimental spectrum.[3]

TABLE VI. Minimum energies of conical intersections (eV) between various low-lying excited singlet states of furan.

	$^1B_2(V)$	$^1B_1(3p)$	$^1A_1(V')$
$^1A_2(3s)$	6.32	>10	6.47
$^1B_2(V)$		6.54	6.38
$^1B_1(3p)$			6.42

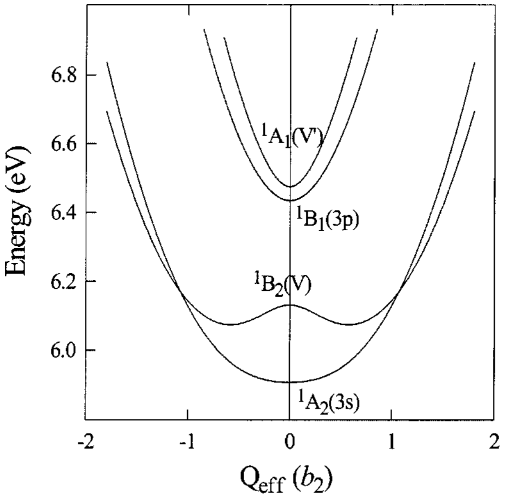

FIG. 2. Cut through the adiabatic PES along an effective coordinate, chosen as a combination of the b_2 coupling modes. The totally symmetric normal coordinates are set to values corresponding to the geometry of the $^1A'(V)$ state (C_s structure).

B. Excitation spectrum

The excitation spectrum of furan calculated using the MCTDH method and all *ab initio* parameters for the present model [Hamiltonian of Eq. (1)] is shown in Fig. 4(b). The theoretical spectrum is compared with the VUV absorption spectrum of Palmer *et al.*,[23] Fig. 4(a). The full theoretical spectral envelope is shown by the bold line and the contributions from the individual vibronic symmetries are shown by the regular lines. Here we note that the A_1 vibronic symmetry cannot be seen in the plot due to the negligibly small oscillator strength of the $V'(^1A_1)$ transition. We also note that the theoretical and experimental spectra are aligned for maximal coincidence. In the following we disregard the energy shifts and discuss only relative excitation energies.

The theoretical spectrum, obtained using only *ab initio* values of the parameters, reproduces qualitatively correctly the VUV spectrum up to about 6.1 eV. According to the present results, complicated multistate/multimode vibronic interactions are responsible for the final appearance of the spectrum. At higher energy the theoretical spectrum begins to differ from the experimental profile. Whereas in the region 6.1–6.4 eV the experimental spectrum is relatively smooth, the corresponding part of the theoretical spectra exhibits pronounced maxima, arising from the contributions of the B_1 vibronic progression. Keeping in mind possible errors of our *ab initio* calculations, one may speculate that the first peak of the B_1 progression correlates with the sharp maximum in the experimental spectrum near 6.5 eV. This would imply that the vertical energy gap between the $^1B_2(V)$ and the $^1B_1(3p)$ states is underestimated in our calculations by 0.25 eV. The latter is quite possible, since the expected accuracy of the EOM-CCSD method with respect to the individual excitation energies is about 0.1–0.2 eV.[57] To check this idea, we performed calculations with an adjusted $3p(^1B_1)$ vertical excitation energy of 6.78 eV. Also we had to discard the interaction terms between $^1B_1(3p)$ and $^1A_1(V')$ states, since they should no longer be valid after the energy adjustment, which reverses the order of these states. The spectrum of this adjusted model [Fig. 4(c)] agrees with experiment distinctly better, especially in the high-energy region. The structures A-G and γ seen in the experimental spectrum can now be readily identified in the theoretical profile. Considering the energy scale it is seen that a better agreement with experiment is possible by shifting up the $3p(^1B_1)$ vertical excita-

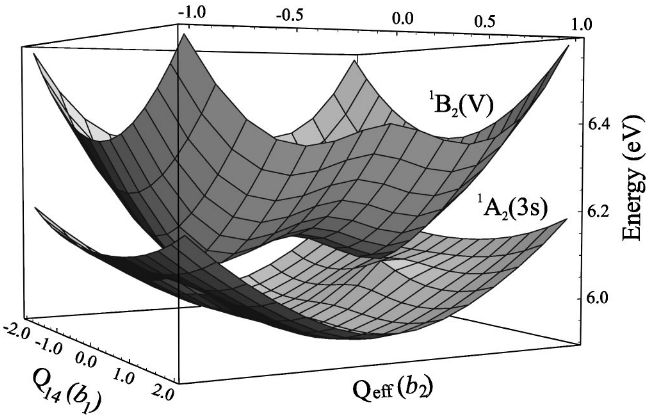

FIG. 3. Three-dimensional view of the $S_1(^1A_2)$ and $S_2(^1B_2)$ PES with respect to an effective coordinate, chosen as a combination of the b_2 modes, and the normal coordinate $Q_{14}(b_1)$. The other normal coordinates are set to values corresponding to the geometry of the $^1A'(V)$ state [for better visibility the $^1B_2(V)$ PES, and hence conical intersection, is shifted down].

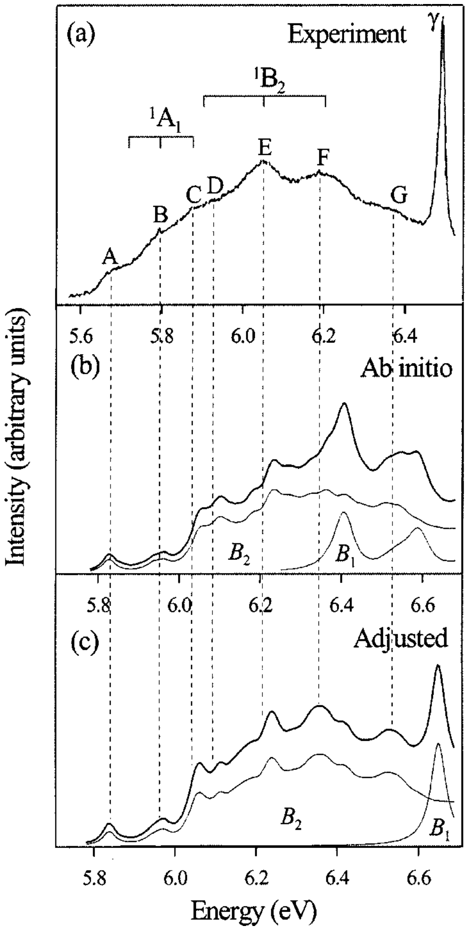

FIG. 4. The lowest photoabsorption band of furan: (a) experimental VUV spectrum of Palmer *et al.* (Ref. 23); (b) *ab initio* model; (c) adjusted model.

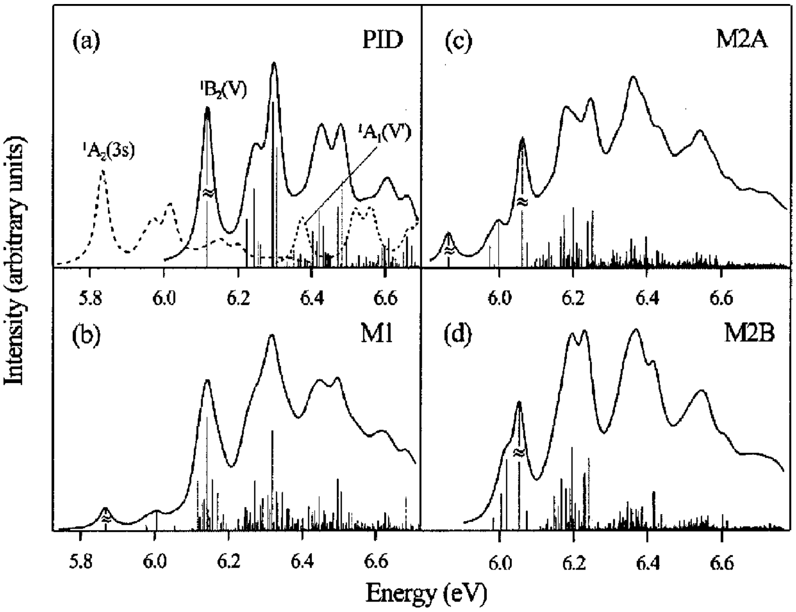

FIG. 5. Analysis of the B_2 vibronic contribution to the lowest photoabsorption band of furan: (a) Poisson intensity distribution [additionally are shown the $^1A_2(3s)$ and $^1A_1(V')$ vibrational progressions which do not contribute to the spectral intensity]; (b) $M1$ model ($^1A_2\times b_1\times {}^1B_2$ coupling); (c) $M2A$ model ($^1A_2\times b_1\times {}^1B_2$ and $^1B_2\times b_2\times {}^1A_1$); (d) $M2B$ model ($^1A_2\times a_2\times {}^1A_1$ and $^1B_2\times b_2\times {}^1A_1$).

tion energy by only 0.08 eV and shifting down the other three excitation energies [for the $^1A_2(3s)$, $^1B_2(V)$, and $^1A_1(V')$ excited states] by 0.17 eV. This does not affect the vibronic structure of Fig. 4(c) in any way, but brings the energy scale into nearly perfect agreement with the experimental one in Fig. 4(a).

1. Analysis of the excitation spectrum

To shed more light on the structure of the VUV spectra, and to clarify the role played by the various coupling schemes, in this subsection we study the spectra of the optically dominant B_2 vibronic symmetry computed using various reduced models. These models are derived from the original (full *ab initio*) model by retaining only one ($M1$ model) or two ($M2X$ models, $X=A$, B, or C) coupling schemes that have the most impact on the spectrum. The spectra are calculated using the time-independent approach employing the Lanczos algorithm which allows for obtaining "bar" spectra, useful for our analysis.

Before studying vibronic coupling spectra it is worthwhile to consider the spectrum of Poisson intensity distribution (PID) (all vibronic couplings are suppressed) which yields useful information about excitation of the totally symmetric modes upon transition to the $^1B_2(V)$ state. The spectrum [Fig. 5(a)] is characterized by excitations of the $\nu_3-\nu_8$ modes, among which the modes ν_3 and ν_4 are most strongly excited. The first seven lines in the PID spectrum are the fundamental 0-0 transition followed by lines corresponding to the excitations of single quanta of the $\nu_3-\nu_8$ modes. The relative positions of these lines in the vibronic coupling spectra usually persist (though their intensities can change), so that they can be used to identify the excitations of the nontotally symmetric modes.

As was shown in Sec. IV A, there is appreciable coupling between the $^1B_2(V)$ and $^1A_2(3s)$ states via the b_1 mode ν_{14}. This suggests that the mode should be strongly excited in the spectrum. The latter is confirmed by the spectrum of the $M1$ model (only the $^1A_2\times b_1\times {}^1B_2$ coupling scheme is taken into account) shown in Fig. 5(b). As can be seen, it differs sharply from the PID spectrum by beginning at much lower energy and exhibiting lines in the energy range 5.8–6.1 eV, absent in the PID spectrum. These are excitations of the b_1 mode ν_{14} associated with the PES of the lower $^1A_2(3s)$ state. In addition, many new vibronic lines arise in the region corresponding to the $^1B_2(V)$ progression. Most of them are seen in the vicinity of the a_1 lines belonging to the $^1B_2(V)$ progression. This effect develops when the dense "tail" of the b_1 progression associated with the lower $^1A_2(3s)$ state overlaps with the excitations of the a_1 modes in the upper $^1B_2(V)$ state, leading to a resonance-like broadening of the a_1 levels. The spectrum becomes very complex above the point of the conical intersection, expected in the $M1$ model at 6.32 eV.

The coupling between the $^1B_2(V)$ and $^1A_1(V')$ states via the b_2 modes has a strong effect on the PES of the $^1B_2(V)$ state (see Sec. IV A). One could thus expect excitations of the b_2 modes in the beginning of $^1B_2(V)$ progression due to the double-well shape of the $^1B_2(V)$ PES along the b_2 coordinates.[3] Within the isolated $^1B_2\times b_2\times {}^1A_1$ coupling scheme such excitations were found to be quite weak and the spectrum resembles the PID one. The situation, however, changes if the $^1A_2\times b_1\times {}^1B_2$ vibronic interaction is simultaneously taken into account ($M2A$ model). The spectrum of the $M2A$ model [Fig. 5(c)] resembles, to some extent, the spectrum of the $M1$ model indicating the leading role of the $^1A_2\times b_1\times {}^1B_2$ interaction. The interesting feature of the $M2A$ spectrum is the group of lines about 6.2 eV, absent in the spectrum of the $M1$ model. These vibronic levels are found to be constructed of a single quantum of the b_1 mode ν_{14}, several quanta of b_2 modes, and the $^1A_2(3s)$ electronic part. The importance of the b_2 modes follows from their tuning role for the intersection of the $^1A_2(3s)$ and $^1B_2(V)$ PES (see Sec. IV A), which means that the excitation of the b_2 modes facilitates the interaction of the electronic states along the b_1 (coupling) mode. The mixing of the b_2

and b_1 modes in our case is thus similar to the mixing of the tuning and coupling modes.[3]

Finally it is important to understand the spectral role of the *indirect* coupling between the ${}^1A_2(3s)$ and ${}^1B_2(V)$ states, mediated by a combination of the a_2 and b_2 modes and involving a third excited state, either the ${}^1A_1(V')$ or the ${}^1B_1(3p)$ state. To this end we analyze the spectrum of the $M2B$ model [Fig. 5(d)] where *indirect* coupling is included by taking simultaneously ${}^1A_2\times a_2\times{}^1A_1$ and ${}^1B_2\times b_2\times{}^1A_1$ interactions into account. The spectrum of the $M2B$ model indicates the presence of extensive vibronic coupling effects. It differs substantially from the spectrum of the PID model exhibiting many new vibronic lines. These are clearly excitations of the nontotally symmetric modes associated with the ${}^1A_2(3s)$ state. Similar vibronic excitations can be seen in the spectra of the $M2A$ and $M1$ models accounting for direct coupling of the ${}^1A_2(3s)$ and ${}^1B_2(V)$ states. However, the direct coupling of these states via the b_1 mode is "switched off" in the $M2B$ model and therefore the observed vibronic satellites are excited solely by the indirect coupling mechanism. The excitations have b_1 symmetry and represent various combinations of the odd number of quanta of the b_2 and a_2 modes. The other scheme of *indirect* coupling through the ${}^1B_1(3p)$ state ($M2C$ model, simultaneous ${}^1A_2\times b_2\times{}^1B_1$ and ${}^1B_2\times a_2\times{}^1B_1$ couplings) was found to give rise to much weaker excitations of the b_2 and a_2 modes than in the case of the $M2B$ model.

2. Assignment of the excitation spectrum

The excitation of furan was the subject of many experimental studies.[9–24] Despite the progress in the understanding of the photoabsorption spectrum, an accurate assignment of its lowest band [Fig. 4(a)] is still not available. Whereas the band maximum at 6.04 eV could be firmly assigned to the valence $V({}^1B_2)$ transition, the interpretation of the progression on its low-energy side is rather controversial. In his review, Robin stated that this progression is either the $3s({}^1A_2)$ Rydberg or the $V'({}^1A_1)$ valence transition.[21] An attempt to clarify the situation was made by Roebber *et al.*[20] who studied the jet-cooled VUV spectrum under conditions leading to formation of the molecular clusters and came to the conclusion that the progression should be assigned to the $V'({}^1A_1)$ valence transition. From their multiphoton ionization spectrum the same authors were able to identify a transition at 5.91 eV, which they assigned to the ${}^1A_2(3s)$ Rydberg state. These assignments were left unchanged in the subsequent VUV studies of Nyulaszi *et al.*[22] and Palmer *et al.*[23]

Although the assignment of the low-energy progression to the $V'({}^1A_1)$ transition is appealing since it is dipole-allowed (and hence can be observed in the photoabsorption), the most recent *ab initio* calculations[8,31,33] do not support this assignment. According to our EOM-CCSD vertical excitation energies in Table I the $3s({}^1A_2)$ is the lowest transition of furan. The $V'({}^1A_1)$ transition is, on the contrary, only the fifth lowest vertical transition. Also, adiabatically the minimum of the ${}^1A_1(V')$ state is predicted at least 0.5 eV above the minimum of the lowest ${}^1A_2(3s)$ state (Paper I). In addition, all calculations predict for the $V'({}^1A_1)$ transition extremely low oscillator strength, so that its direct influence on the photoabsorption profile should be nearly negligible. The same is true for the $3s({}^1A_2)$ transition, which is strictly optically forbidden. If these predictions are correct, how then the $3s({}^1A_2)$ transition can be seen in the VUV spectrum, and how to explain the valence character of the observed structure? We believe that our present results answer these questions.

As it was suggested in Ref. 29, vibronic interaction with dipole-allowed transitions can make certain levels of the ${}^1A_2(3s)$ progression visible in the VUV spectrum via intensity-borrowing mechanisms. The present calculations confirm this suggestion. The low-energy flank of the theoretical spectrum [Fig. 4(c)] shows low-intensity structure, absent in the PID case [Fig. 5(a)]. As shown above, the nontotally symmetric b_1 modes and the combinations of b_2 and a_2 modes are excited in the ${}^1A_2(3s)$ state due to the vibronic coupling of this state to the higher-lying ${}^1B_2(V)$ and ${}^1A_1(V')$ states. These excitations comprise the very lowest portion of the spectrum (energy region 5.8–6.0 eV), where the adiabatic picture is still valid. The final vibronic states ${}^1A_2\times b_1$ and ${}^1A_2\times a_2\times b_2$ belong to the B_2 symmetry and acquire VUV intensity from the strongly optically allowed valence transition $V({}^1B_2)$. This example of the intensity borrowing is remarkable since here the vibronic interaction mixes states of Rydberg $[{}^1A_2(3s)]$ and valence $[{}^1B_2(V)$ and ${}^1A_1(V')]$ character. Such valence-Rydberg mixing is in agreement with the observation of certain valence character in the discussed spectral region. For the VUV profile in Fig. 4(a) our findings would imply that the former assignment of the features A-C to the $V'({}^1A_1)$ transition[20,22,23] should be revised. The shoulders A and B have to be assigned to excitations of the nontotally symmetric modes in the ${}^1A_2(3s)$ Rydberg state borrowing their intensity from the valence ${}^1B_2(V)$ state. Whereas shoulder A is exclusively due to the excitation of the b_1 modes, shoulder B contains contributions of the more complex "b_2 plus a_2" type (Sec. IV B 1).

Strong nonadiabatic effects can be expected in the excitation spectrum above the conical intersection of the S_1 and S_2 PES. According to our calculations this intersection takes place at about 6.07–6.18 eV, which corresponds to an energy of 5.83–5.94 eV in the experimental spectrum. As is well known,[3,4] above this region the nuclear dynamics no longer proceeds on the individual PES, so that the features C-G cannot be strictly assigned to any single electronic state. The assignment of the band maximum E and the features D and F to the ${}^1B_2(V)$ state[20–23] is therefore only partly correct, and should be understood in such a way that the ${}^1B_2(V)$ represents here the main source of intensity. Though within the PID approximation the experimental band maximum indeed corresponds to the maximum of the ${}^1B_2(V)$ progression [Fig. 5(a)], the latter is strongly modified by the interaction with the lower-lying ${}^1A_2(3s)$ and higher-lying ${}^1A_1(V')$ states.

Our results support the assignments of the sharp peak γ at 6.48 eV to the 0-0 line of the $3p({}^1B_1)$ transition. This transition was first clearly observed and assigned by Cooper *et al.*[19] in the resonantly enhanced multiphoton ionization (REMPI) experiment. The $3p({}^1B_1)$ transition is seen so well in the VUV spectrum, since it has the second largest optical

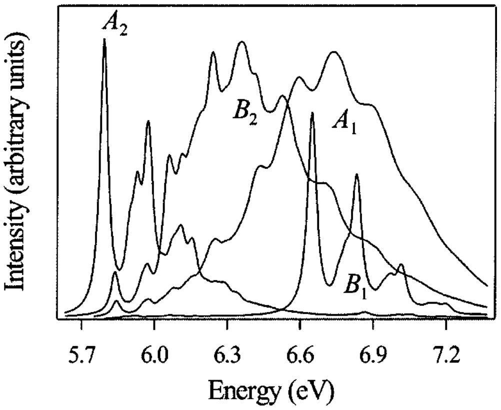

FIG. 6. Contributions of the A_1, A_2, B_1, and B_2 vibronic symmetries to the low-energy part of the excitation spectrum of furan (results of the adjusted model). The A_1 and A_2 spectra are plotted with arbitrary electron intensity, chosen for optimal visibility.

oscillator strength in the considered energy region after the valence $V(^1B_2)$ transition.

In the present section we have dealt with the VUV spectrum of furan, which according to the oscillator strength factors is mainly determined by the vibronic progressions of the B_2 and B_1 symmetry. The vibronic excitations of the A_2 and A_1 symmetry were not discussed so far. However, they can become also important in other type of experiments. As seen in Fig. 6, where the vibronic progressions of all symmetries are shown, the progressions reside virtually on top of each other and span a considerable energy range. The VUV spectrum is obtained when the vibronic B_2 symmetry dominates. However, as can be easily verified, a spectral envelope quite different from the VUV absorption profile arises, if the relative importance of the vibronic symmetries will be changed. This can happen when an excitation mechanism different from the gas-phase photoabsorption (i.e., governed by a different or modified electronic transition operator) is employed. Into this category fall, for example, electron energy loss spectroscopy and all experiments carried out under specific (e.g., solid or liquid-state) conditions. It should be clear that all such experiments will manipulate the entire spectrum, and not only the individual transitions, as it is often wrongly assumed in the experimental literature. This is therefore likely to be another source of the controversial assignments in the spectroscopy of furan and related heterocyclic molecules.

C. Population dynamics

In this section we discuss the femtosecond internal conversion (IC) dynamics of excited furan. In Fig. 7 we show the time evolution of the excited-state population after transition to the $^1B_2(V)$ state, computed using the *ab initio* and adjusted models. They yield qualitatively similar dynamics, predicting that the populations of the $^1A_2(3s)$, $^1B_2(V)$, and $^1A_1(V')$ states undergo profound changes in time, whereas the population of the $^1B_1(3p)$ state remains relatively constant, that is, resembles a "heat bath." In the following we therefore restrict our discussion to the former three states.

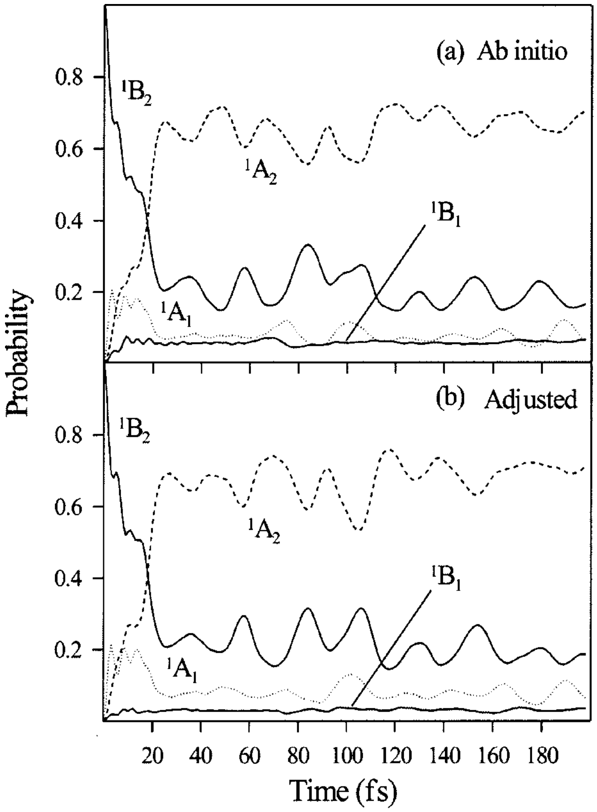

FIG. 7. Time evolution of the excited-state populations: (a) *ab initio* model, (b) adjusted model.

The prominent feature of the population plots in Fig. 7 is the ultrafast decay of the $^1B_2(V)$ state on the time scale of about 25 fs. In this time the $^1B_2(V)$ state loses about 80% of its population, which is mostly transferred to the $^1A_2(3s)$ state. In the first few femtoseconds the decay is accompanied by an abrupt growth of population of the $^1A_1(V')$ state. This indicates the role of the $^1A_1(V')$ state in the intersection of the $S_1(^1A_2)$ and $S_2(^1B_2)$ PES. The relative population of the $^1A_1(V')$ state rises to about 20%, and after 15 fs goes down. At 20 fs it reaches 10% and oscillates around this value at larger times. The population of the $^1A_2(3s)$ state grows nearly monotonously and reaches its maximum of about 70% at 25 fs. The $^1B_2(V)$ state at this time is populated only to about 20%. At longer times the population curves exhibit beats due to recrossing of the wave packet from the $^1A_2(3s)$ to the $^1B_2(V)$ state.

To better understand the above IC process we take a look at the population dynamics within the auxiliary models $M1$ ($^1A_2 \times b_1 \times {}^1B_2$ coupling), $M2A$ ($^1A_2 \times b_1 \times {}^1B_2 + {}^1B_2 \times b_2 \times {}^1A_1$), $M2B$ ($^1A_2 \times a_2 \times {}^1A_1 + {}^1B_2 \times b_2 \times {}^1A_1$), and $M2C$ ($^1A_2 \times b_2 \times {}^1B_1 + {}^1B_2 \times a_2 \times {}^1B_1$) shown in Fig. 8. As expected, the interaction of the $^1A_2(3s)$ and $^1B_2(V)$ states plays central role in the IC process. This should be clear from the population plots of the $M1$ model [Fig. 8(a)]. This model accounts for just the above two states, but qualitatively yields similar dynamics as in the more accurate *ab initio* and adjusted models. The IC from the $^1B_2(V)$ to the $^1A_2(3s)$ state proceeds through the conical intersection of the $S_1(^1A_2)$ and $S_2(^1B_2)$ PES and is accomplished within about 20 fs (time in which the population of the two states

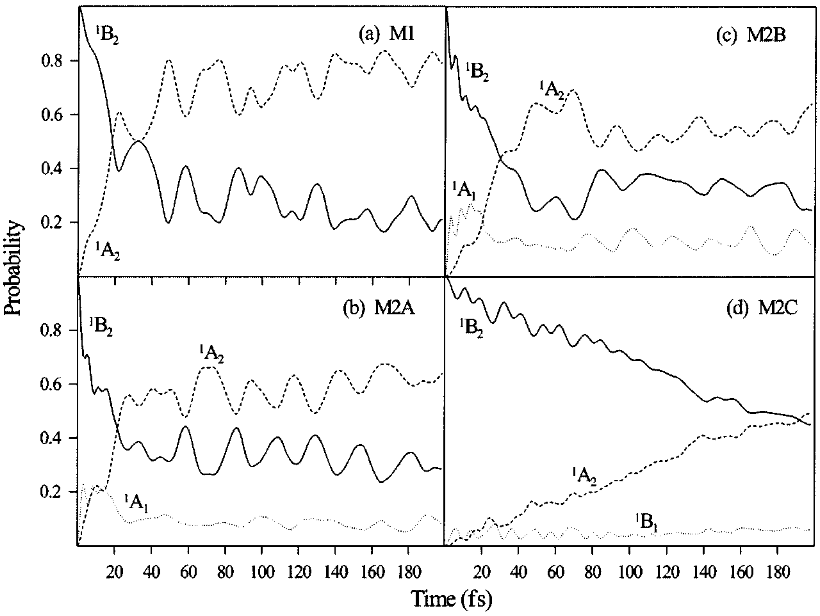

FIG. 8. Analysis of time evolution of the excited-state populations: (a) $M1$ model ($^1A_2 \times b_1 \times {}^1B_2$ coupling); (b) $M2A$ model ($^1A_2 \times b_1 \times {}^1B_2$ and $^1B_2 \times b_2 \times {}^1A_1$); (c) $M2B$ model ($^1A_2 \times a_2 \times {}^1A_1$ and $^1B_2 \times b_2 \times {}^1A_1$); (d) $M2C$ model ($^1A_2 \times b_2 \times {}^1B_1$ and $^1B_2 \times a_2 \times {}^1B_1$).

becomes equal). This ultrafast decay time is determined by the periods of the dominant totally symmetric modes [in the $^1B_2(V)$ state]. These are the modes ν_3, ν_4, and ν_7 with periods in the range of 20–30 fs.

Within the $M2A$ model [Fig. 8(b)] the conical intersection of the $S_1(^1A_2)$ and $S_2(^1B_2)$ PES involves interaction with the $^1A_1(V')$ state via b_2 modes. Some of the $^1B_2(V)$ population is therefore transferred to the $^1A_1(V')$ state. The latter is populated to about 12%, when the $^1B_2(V)$ and $^1A_2(3s)$ states are equally populated at the level of 44%. This implies 56% population loss for the $^1B_2(V)$ state, which is less than in the *ab initio* and adjusted models. This indicates the existence of an additional decay channel in those models.

Such a channel represents the conical intersection of the S_1 and S_2 PES due to the *indirect* coupling mechanism (Secs. IV A and IV B 1). This coupling is realized either with the $^1A_1(V')$, or with the $^1B_1(3p)$ state ($M2B$ and $M2C$ models, respectively). The population dynamics of the $M2B$ model [Fig. 8(c)] qualitatively resembles the case of the direct coupling involving the same electronic states [results of $M2A$ model in Fig. 8(b)]. The main difference is that the IC proceeds now somewhat slower. The $M2C$ model yields a quite different dynamical picture [Fig. 8(d)] characterized by a very slow population transfer from the $^1B_2(V)$ to the $^1A_2(3s)$ state. This happens because the indirect coupling via the $^1B_1(3p)$ state is much weaker than via the $^1A_1(V')$ state and does not lead to a low-lying conical intersection.

IV. SUMMARY AND CONCLUSIONS

In the present work we have studied the spectra and molecular dynamics of furan, related to the manifold of its low-lying excited states $^1A_2(3s)$, $^1B_2(V)$, $^1A_1(V')$, and $^1B_1(3p)$. An adequate quantum-dynamical approach was employed. The information on the excited-state PES was obtained from the *ab initio* calculations (Paper I). A realistic LVC model Hamiltonian describing the excited-state nuclear dynamics was formulated based on the results of these calculations. The resulting Hamiltonian was used for the calculation of the excitation spectra and evaluation of the population dynamics. The latter task was accomplished by using the Heidelberg MCTDH package.[40]

Our work establishes that the low-lying excited singlet states of furan represent a genuinely complex vibronic coupling system. The four states $^1A_2(3s)$, $^1B_2(V)$, $^1A_1(V')$, and $^1B_1(3p)$ have to be treated together to ensure a reliable description of the nuclear dynamics. Under the LVC approximation the most important interactions are simultaneous couplings $^1B_2 \times b_2 \times {}^1A_1$ and $^1A_2 \times b_1 \times {}^1B_2$ leading to a low-lying conical intersection of the $S_1(^1A_2)$ and $S_2(^1B_2)$ PES, taking place in the space of the a_1, b_1, and b_2 vibrational coordinates. An interesting finding of the present study is that besides the above *direct* coupling of the $^1A_2(3s)$ and $^1B_2(V)$ states, there is also an important *indirect* coupling of these states via combination of the a_2 and b_2 modes: $^1A_2 \times [a_2 \times b_2] \times {}^1B_2$. The latter becomes possible within the LVC scheme due to the $^1A_1(V')$ and $^1B_1(3p)$ states, which mediate this coupling. The indirect coupling also gives rise to the conical intersection of the $S_1(^1A_2)$ and $S_2(^1B_2)$ PES, which now takes place in the space of a_1, a_2, and b_2 coordinates.

The theoretical photoabsorption spectrum of furan computed using purely *ab initio* parameters in the LVC model Hamiltonian (*ab initio* model) is in a good qualitative agreement with the experimental VUV spectrum.[23] The agreement with experiment improves when the vertical excitation energy of the $3p(^1B_1)$ transition is increased by about 0.25 eV (adjusted model). The obtained spectrum is still shifted with respect to the experimental one by about 0.17 eV to higher energy, which indicates that the present EOM-CCSD vertical excitation energies for the $3s(^1A_2)$, $V(^1B_2)$, and $V'(^1A_1)$ transitions are about 0.17 eV too high and the energy of the $3p(^1B_1)$ transition is about 0.08 eV too low.

The complex excited-state vibronic effects make assignments of the photoabsorption spectrum very difficult. Nevertheless, at the qualitative level, our results answer several important questions. The weak structure on the low-energy side of the lowest photoabsorption band represents excitations of the b_1 and b_2 plus a_2 vibrational modes in the ${}^1A_2(3s)$ state. Interpretation in terms of the individual PES here is valid, since this part of the spectrum is still below the energy of the lowest conical intersection, predicted to occur at 5.83–5.94 eV in the experimental spectrum. The ${}^1A_2 \times b_1$ and ${}^1A_2 \times b_2 \times a_2$ vibronic transitions get their photoabsorption intensity from the strongly dipole-allowed $V({}^1B_2)$ transition. In turn, these levels acquire some valence character of the ${}^1B_2(V)$ state, what might have misled previous experimental studies to assigning them to the valence ${}^1A_1(V')$ type. The structure above 5.9 eV cannot be interpreted anymore in terms of single PES, as there a strongly nonadiabatic regime sets in. The total number of spectral lines exceeds the expectation based on uncoupled surfaces [PID spectrum of Fig. 5(a)] by ~2 orders of magnitude. The traditional assignment of the band maximum at about 6.06 eV to the $V({}^1B_2)$ transition should therefore be understood in such a way that the ${}^1B_2(V)$ state plays here the role of the main source of the spectral intensity. Our results support the assignments[19] of the sharp peak in the experimental spectrum at 6.48 eV to the 0-0 line of the $3p({}^1B_1)$ transition.

The present study of the excited-state dynamics supports the picture proposed in Paper I for internal conversion from the ${}^1B_2(V)$ state: As soon as the system reaches the ${}^1B_2(V)$ state (C_{2v} saddle point of S_2 PES), it begins to relax along the b_2 coordinate. This is an in-plane distortion triggered by interaction of the ${}^1B_2(V)$ and ${}^1A_1(V')$ states (Fig. 2). Accordingly, the population of the latter state rapidly increases to about 20% and remains at this level for about 15 fs before it drops. The relaxation proceeds along the b_2 coordinate through the conical intersection of the S_1 and S_2 PES, and brings the system to the ${}^1A'(V)$ state (C_s saddle point of the S_1 PES). In this phase the population of the ${}^1A_2(3s)$ state steadily increases, whereas the population of the ${}^1B_2(V)$ state concertedly decreases. Already at 20 fs the ${}^1B_2(V)$ and ${}^1A_2(3s)$ states become equally populated, the ${}^1B_2(V)$ state retaining only 40% of its initial population. Since the ${}^1A'(V)$ structure is itself a saddle point with respect to out-of-plane deformation (Fig. 3), the relaxation continues along b_1 and a_2 modes on the S_1 surface. Finally, the relaxation brings the system to the bottom of the S_1 PES (C_{2v} minimum), that is, to the ${}^1A_2(3s)$ sate. The relaxation process is accomplished within 25 fs, when the populations of the ${}^1A_2(3s)$ and ${}^1B_2(V)$ states reach their maximal and minimal levels of about 70% and 20%, respectively. This femtosecond process is another example of ultrafast internal conversion dynamics triggered by conical intersections of potential energy surfaces.[7]

In conclusion, we note once again that the (*direct* and *indirect*) vibronic interaction of the ${}^1A_2(3s)$ and ${}^1B_2(V)$ states is by far the most important factor triggering the ultrafast internal conversion to the ${}^1A_2(3s)$ state and the nonadiabatic effects in the excitation spectrum of furan at low energy. Similar effects can be expected in the case of related heterocyclic molecules.

ACKNOWLEDGMENTS

This work was supported by the *Russian Foundation for Basic Research* (RFBR) and by the *Deutsche Forschungsgemeinschaft* (DFG). Two of the authors (E.V.G. and A.B.T.) are grateful for the hospitality and support during their stay in the Heidelberg Theoretical Chemistry Group. The authors are indebted to W. Domcke for his interest in this work and for valuable discussions.

APPENDIX: ANALYSIS OF THE INDIRECT COUPLING MECHANISM

In the present Appendix we demonstrate the mechanism of the *indirect* coupling of the ${}^1A_2(3s)$ and ${}^1B_2(V)$ states via combination of the a_2 and b_2 modes (${}^1A_2 \times [a_2 \times b_2] \times {}^1B_2$). Let us consider as an example the Hamiltonian with the potential energy part:

$$\mathbf{U}=\begin{pmatrix} E(A_2)+\sum\limits_{s\in a_1} k_s^1 Q_s & \sum\limits_{s\in b_1} \lambda_s^{12} Q_s & \sum\limits_{s\in a_2} \lambda_s^{13} Q_s \\ \sum\limits_{s\in b_1} \lambda_s^{12} Q_s & E(B_2)+\sum\limits_{s\in a_1} k_s^2 Q_s & \sum\limits_{s\in b_2} \lambda_s^{23} Q_s \\ \sum\limits_{s\in a_2} \lambda_s^{13} Q_s & \sum\limits_{s\in b_2} \lambda_s^{23} Q_s & E(A_1)+\sum\limits_{s\in a_1} k_s^3 Q_s \end{pmatrix}. \tag{A1}$$

The eigenvalue problem for the 3×3 matrix $\mathbf{U}$, given by the equation $\mathbf{U}\vec{\mathbf{X}}=u\vec{\mathbf{X}}$ (where u and $\vec{\mathbf{X}}$ are, respectively, an eigenvalue and its eigenvector) can be reduced to the eigenvalue problem $\tilde{\mathbf{U}}\vec{\tilde{\mathbf{X}}}=u\vec{\tilde{\mathbf{X}}}$ for a 2×2 matrix $\tilde{\mathbf{U}}$ using partitioning techniques. The eigenvector $\vec{\tilde{\mathbf{X}}}$ is given by the first two components of the original eigenvector $\vec{\mathbf{X}}$ for the same eigenvalue u. The new matrix $\tilde{\mathbf{U}}$ is defined as follows:

$$\tilde{\mathbf{U}}=\begin{pmatrix} E(A_2)+\sum_{s\in a_1} k_s^1 Q_s & \sum_{s\in b_1}\lambda_s^{12}Q_s \\ \sum_{s\in b_1}\lambda_s^{12}Q_s & E(B_2)+\sum_{s\in a_1}k_s^2 Q_s \end{pmatrix} + \left(u-E(A_1)-\sum_{s\in a_1}k_s^3 Q_s\right)^{-1}\begin{pmatrix} \left\{\sum_{s\in a_2}\lambda_s^{13}Q_s\right\}^2 & \sum_{r\in a_2}\sum_{s\in b_2}\lambda_r^{13}\lambda_s^{23}Q_rQ_s \\ \sum_{r\in a_2}\sum_{s\in b_2}\lambda_r^{13}\lambda_s^{23}Q_rQ_s & \left\{\sum_{s\in b_2}\lambda_s^{23}Q_s\right\}^2 \end{pmatrix} \qquad \text{(A2)}$$

and depends on the eigenvalue u under consideration. The first term on the right-hand side of Eq. (A2) is the familiar *direct* coupling of the ${}^1A_2(3s)$ and ${}^1B_2(V)$ states. The second term explicitly depends on the product of normal coordinates of the a_2 and b_2 symmetry, and can be interpreted as *indirect* coupling of the ${}^1A_2(3s)$ and ${}^1B_2(V)$ states. It is interesting to note that as follows from the factor $[u-E(A_1)-\Sigma_{s\in a_1}k_s^3Q_s]^{-1}$, the indirect coupling depends also on the energy of the third state, ${}^1A_1(V')$, and on the totally symmetric coordinates.

[1] A. H. Zewail, *Femtochemistry, Ultrafast Dynamics of the Chemical Bond*, World Scientific Series in the 20th Century Vols. 1 and 2 (World Scientific, Singapore, 1994); *Femtochemistry—Ultrafast Chemical and Physical Processes in Molecular Systems*, edited by M. Chergui (World Scientific, Singapore, 1996).

[2] W. Domcke and G. Stock, Adv. Chem. Phys. **100**, 1 (1997).

[3] H. Köppel, W. Domcke, and L. S. Cederbaum, Adv. Chem. Phys. **57**, 59 (1984).

[4] H. Köppel and W. Domcke, in *Encyclopedia of Computational Chemistry*, edited by P. von Ragué (Wiley, New York, 1998), p. 3166; H. Köppel, W. Domcke, and L. S. Cederbaum, in *Conical Intersections: Electronic Structure, Dynamics and Spectroscopy* [Ref. 7(b)], p. 313.

[5] I. B. Bersuker and V. Z. Polinger, *Vibronic Interactions in Molecules and Crystals* (Springer, Berlin, 1989); I. B. Bersuker, Chem. Rev. (Washington, D.C.) **101**, 1067 (2001).

[6] D. R. Yarkony, J. Phys. Chem. A **105**, 6277 (2001); D. R. Yarkony, Rev. Mod. Phys. **68**, 985 (1996).

[7] (a) Chem. Phys. **259**, 121 (2000) (special issue on conical intersections), edited by Y. Haas, M. Klessinger, S. Zilberg; (b) *Conical Intersections: Electronic Structure, Dynamics and Spectroscopy*, edited by W. Domcke, D. Yarkony, and H. Köppel (World Scientific, Singapore, 2004).

[8] E. V. Gromov, A. B. Trofimov, N. M. Vitkovskaya, J. Schirmer, and H. Köppel, J. Chem. Phys. **119**, 737 (2003).

[9] L. W. Picket, J. Chem. Phys. **8**, 293 (1940).

[10] W. C. Price and A. D. Walsh, Proc. R. Soc. London, Ser. A **179**, 201 (1941).

[11] L. W. Pickett, N. J. Hoeflich, and T.-C. Liu, J. Am. Chem. Soc. **73**, 4865 (1951).

[12] K. Watanabe and T. Nakayama, J. Chem. Phys. **29**, 48 (1958).

[13] G. Horvath and Å. I. Kiss, Spectrochim. Acta, Part A **23A**, 921 (1967).

[14] P. J. Derrick, L. Åsbrink, O. Edqvist, B.-Ö. Jonsson, and E. Lindholm, Int. J. Mass Spectrom. Ion Phys. **6**, 161 (1971).

[15] E. H. van Veen, Chem. Phys. Lett. **41**, 535 (1976).

[16] W. M. Flicker, O. A. Mosher, and A. Kuppermann, Chem. Phys. Lett. **38**, 489 (1976); W. M. Flicker, O. A. Mosher, and A. Kuppermann, J. Chem. Phys. **64**, 1315 (1976).

[17] B. Nordén, R. Håkansson, P. B. Pedersen, and E. W. Thulstrup, Chem. Phys. **33**, 355 (1978).

[18] L. Sanche, J. Chem. Phys. **71**, 4860 (1979).

[19] C. D. Cooper, A. D. Williamson, J. C. Miller, and R. N. Compton, J. Chem. Phys. **73**, 1527 (1980).

[20] J. L. Roebber, D. P. Gerrity, R. Hemley, and V. Vaida, Chem. Phys. Lett. **75**, 104 (1980).

[21] M. B. Robin, *Higher Excited States of Polyatomic Molecules* (Academic Press, New York, 1975), Vol. 2; (Academic Press, New York, 1985), Vol. 3.

[22] L. Nyulászi, J. Mol. Struct. **273**, 133 (1992).

[23] M. H. Palmer, I. C. Walker, C. C. Ballard, and M. F. Guest, Chem. Phys. **192**, 111 (1995).

[24] O. Sorkhabi, F. Qi, A. H. Rizvi, and A. G. Suits, J. Chem. Phys. **111**, 100 (1999).

[25] K.-H. Thunemann, R. J. Buenker, and W. Butscher, Chem. Phys. **47**, 313 (1980).

[26] H. Nakatsuji, O. Kitao, and T. Yonezawa, J. Chem. Phys. **83**, 723 (1985).

[27] L. Serrano-Andrés, M. Merchán, I. Nebot-Gil, B. O. Roos, and M. Fülscher, J. Am. Chem. Soc. **115**, 6184 (1993).

[28] H. Nakano, T. Tsuneda, T. Hashimoto, and K. Hirao, J. Chem. Phys. **104**, 2312 (1996).

[29] A. B. Trofimov and J. Schirmer, Chem. Phys. **224**, 175 (1997).

[30] O. Christiansen, A. Halkier, H. Koch, and P. Jørgensen, J. Chem. Phys. **108**, 2801 (1998).

[31] O. Christiansen and P. Jørgensen, J. Am. Chem. Soc. **120**, 3423 (1998).

[32] M. D'Auria, J. Org. Chem. **65**, 2494 (2000).

[33] J. Wan, J. Meller, M. Hada, M. Ehara, and H. Nakatsuji, J. Chem. Phys. **113**, 7853 (2000).

[34] R. Burcl, R. D. Amos, and N. C. Handy, Chem. Phys. Lett. **355**, 8 (2002).

[35] A. B. Trofimov, H. Köppel, and J. Schirmer, J. Chem. Phys. **109**, 1025 (1998).

[36] G. A. Worth, H.-D. Meyer, and L. S. Cederbaum, J. Chem. Phys. **105**, 4412 (1996); A. Raab, G. A. Worth, H.-D. Meyer, and L. S. Cederbaum, *ibid.* **110**, 936 (1999).

[37] (a) S. Mahapatra, L. S. Cederbaum, and H. Köppel, J. Chem. Phys. **111**, 10452 (1999); (b) S. Mahapatra, G. A. Worth, H.-D. Meyer, L. S. Cederbaum, and H. Köppel, J. Phys. Chem. A **105**, 5567 (2001).

[38] C. Cattarius, G. A. Worth, H.-D. Meyer, and L. S. Cederbaum, J. Chem. Phys. **115**, 2088 (2001).

[39] H. Köppel, M. Döscher, I. Bâldea, and H.-D. Meyer, J. Chem. Phys. **117**, 2657 (2002).

[40] G. A. Worth, M. H. Beck, A. Jäckle, and H.-D. Meyer, The MCTDH Package, Version 8.2, 2000, http://www.pci.uni-heidelberg.de/tc/usr/mctdh/

[41] H.-D. Meyer, U. Manthe, and L. S. Cederbaum, Chem. Phys. Lett. **165**, 73 (1990); U. Manthe, H.-D. Meyer, and L. S. Cederbaum, J. Chem. Phys. **97**, 3199 (1992).

[42] M. H. Beck, A. Jäckle, G. A. Worth, and H.-D. Meyer, Phys. Rep. **324**, 1 (2000); H.-D. Meyer and G. A. Worth, Theor. Chem. Acc. **109**, 251 (2003).

[43] M. Nest and H.-D. Meyer, J. Chem. Phys. **119**, 24 (2003).

[44] H. Wang, J. Chem. Phys. **113**, 9948 (2000).

[45] H. Wang, M. Thoss, and W. H. Miller, J. Chem. Phys. **115**, 2979 (2001); **115**, 2991 (2001).

[46] H. Wang and M. Thoss, J. Chem. Phys. **119**, 1289 (2003).

[47] W. Lichten, Phys. Rev. **131**, 229 (1963); **139**, A27 (1965); **164**, 131 (1967); F. T. Smith, *ibid.* **179**, 111 (1969); T. F. O'Malley, Adv. At. Mol. Phys. **7**, 223 (1971); T. Pacher, L. S. Cederbaum, and H. Köppel, Adv. Chem. Phys. **84**, 293 (1993).

[48] The dimensionless normal coordinates Q_s are obtained from those of Wilson *et al.* (Ref. 49) by multiplying with $\sqrt{\omega_s}$ (where ω_s is the ground-state vibrational frequency for mode ν_s).

[49] E. B. Wilson, Jr., J. C. Decius, and P. C. Cross, *Molecular Vibrations* (McGraw-Hill, New York, 1955).

[50] L. S. Cederbaum and W. Domcke, Adv. Chem. Phys. **36**, 205 (1977).

[51] J. F. Stanton and R. J. Bartlett, J. Chem. Phys. **98**, 7029 (1993).

[52] T. H. Dunning, Jr., J. Chem. Phys. **90**, 1007 (1989).

[53] A. Mellouki, J. Liévin, and M. Herman, Chem. Phys. **271**, 239 (2001).

[54] A. B. Trofimov, T. E. Moskovskaya, E. V. Gromov, H. Köppel, and J. Schirmer, Phys. Rev. A **64**, 022504 (2001).

[55] J. C. Light, I. P. Hamilton, and J. V. Lill, J. Chem. Phys. **82**, 1400 (1985).

[56] The intersection is also of the conical type because it occurs for finite values of the coordinates of the b_2 modes and, thus, the off-diagonal terms in the effective interaction matrix of Eq. (A2) are effectively linear in the a_2-mode coordinate.

[57] H. Koch, O. Christiansen, P. Jørgensen, and J. Olsen, Chem. Phys. Lett. **244**, 75 (1995); O. Christiansen, H. Koch, P. Jørgensen, and J. Olsen, *ibid.* **256**, 185 (1996).